

Article

Effect of Laser Power on the Recrystallization Temperature of an Additively Manufactured IN718

Deuk Hyun Son ^{1,2}, In Soo Kim ², Baig-Gyu Choi ², Jeonghyeon Do ², Yoon Suk Choi ^{1,*} and Joong Eun Jung ^{2,*}

¹ School of Materials Science and Engineering, Pusan National University, Busan 46241, Republic of Korea; dhson0929@naver.com

² High Temperature Materials Research Group, Korea Institute of Materials Science, Changwon 51508, Republic of Korea; kis@kims.re.kr (I.S.K.); choibg@kims.re.kr (B.-G.C.); jhdo84@kims.re.kr (J.D.)

* Correspondence: choiys@pusan.ac.kr (Y.S.C.); diskbios@kims.re.kr (J.E.J.); Tel.: +82-51-510-2382 (Y.S.C.); +82-55-280-3491 (J.E.J.)

Abstract: Over the past few decades, there has been much research on additive manufacturing in both the academic and the industrial spheres to overcome the limitations of conventional manufacturing methods, thereby enabling the production of complex designs for improved performance. To achieve this purpose, it is crucial to meticulously set suitable laser parameters within the context of microstructural characteristics, including type and fraction of defects, texture development, residual stress, and grain size, etc. In the present study, we focused on recrystallization behavior, a type of relaxation process for accumulated thermal stress during the L-PBF process, as a function of laser power applied on the L-PBF process. The laser power has significant effects on the amount of recrystallized grain, directly related to the recrystallization temperature. Within the range of laser power used in this study, a downward trend was observed in the recrystallization temperature as the laser power increased from 370 W to 390 W. This trend suggests that higher laser power leads to a faster cooling rate, influenced by the volume of melt pool as well as the amount of heat dissipation from the melt pool, resulting in higher thermal stress during the process.

Keywords: recrystallization temperature; driving force for recrystallization during laser powder bed fusion; laser powder bed fusion; IN718; thermal stress



Citation: Son, D.H.; Kim, I.S.; Choi, B.-G.; Do, J.; Choi, Y.S.; Jung, J.E. Effect of Laser Power on the Recrystallization Temperature of an Additively Manufactured IN718. *Metals* **2023**, *13*, 1355. <https://doi.org/10.3390/met13081355>

Academic Editors: Antonello Astarita, Ehsan Hosseini and Vera Popovich

Received: 7 June 2023
Revised: 5 July 2023
Accepted: 25 July 2023
Published: 28 July 2023



Copyright: © 2023 by the authors. Licensee MDPI, Basel, Switzerland. This article is an open access article distributed under the terms and conditions of the Creative Commons Attribution (CC BY) license (<https://creativecommons.org/licenses/by/4.0/>).

1. Introduction

Additive manufacturing of metallic materials has recently drawn much interest in both research and industrial fields due to its potential applications in various high-value-added components, such as gas turbine components, cranial prostheses, dental implants, and more [1–3]. In particular, fabrication of gas turbine components through additive manufacturing can reduce time and cost compared to conventional methods, while enhancing performance of the components. Therefore, gas turbine original equipment manufacturers (OEMs) are actively conducting research on additive manufacturing of Ni-based superalloys, Ti alloys, and Co alloys with various manufacturing techniques, such as laser powder bed fusion (L-PBF), direct energy deposition (DED), and electron beam melting (EBM) [2,4–7]. Among the precipitation-strengthened alloys, the IN718 alloy could provide excellent weldability due to its low Al and Ti content. In addition, it is widely versatile due to its superior heat resistance and oxidation resistance, making it the subject of extensive research in additive manufacturing of Ni-based superalloys.

Energy density is widely used in different forms by researchers, but it is mostly employed in the design of manufacturing processes for fabrication of structures with optimal density, predicting the types of defects that arise during additive manufacturing [8–10]. However, a higher density of a material does not necessarily guarantee

superior mechanical properties, such as tensile strength, creep life, and ductility. The mechanical properties of an additively manufactured material are influenced not only by the fraction of the defect but also by factors such as texture, dislocation density, grain size, and so on. One of the crucial phenomena of microstructural evolution is recrystallization [11,12]. It is the thermal stress or dislocation formed during the process that acts as the driving force for recrystallization of the material [13,14]. As a result, numerous strain-free grains are formed which have a considerable effect on the strength and ductility of materials [15–17]. Recently, the effects of volumetric energy density (VED) on the density, grain morphology, and residual stress variations of L-PBF IN718 across a wide range of 29 to 177 J/mm³ have been reported with the analysis of lattice distortion and residual stress by using EBSD and XRD techniques [18,19]. With increasing VED, lattice distortion was found to increase, leading to a general tendency of increased KAM (kernel average misorientation) values in EBSD analyses. Furthermore, researchers interpreted the occurrence of residual stress in the as-built state as a result of thermal gradients during the additive manufacturing process. A notable finding in these results is that as VED increased in the range of 38 to 90 J/mm³, the residual stress also increased. The edges of the specimens exhibited residual stresses approximately two to five times higher than those in the central regions, indicating that a higher cooling rate promoted higher residual stress. However, the effects of laser parameters on the driving force for recrystallization as well as the recrystallization temperature of additively manufactured IN718 has not been clarified to date. Previous reports did not analyze the changes in recrystallization temperature according to VED or laser parameters. Given that international standards, such as ASTM and AMS, provide guidelines for stress-relief heat treatment conditions for L-PBF IN718, it is essential to investigate the variations in recrystallization temperature with respect to laser parameters. Therefore, this study attempts to investigate the effect of laser power on the driving force for the recrystallization, which in turn affects the recrystallization temperature of additively manufactured IN718.

2. Materials and Methods

IN718 Powder and Laser Powder Bed Fusion

The spherical IN718 powders with sizes ranging from 15 to 53 µm, manufactured by AP&C with the electrode inert gas atomization (EIGA) process, were used. The chemical composition of the IN718 powder is shown in Table 1.

Table 1. Chemical composition of IN718 powder.

| Wt. % | C | Cr | Co | Mo | Nb | Ti | Al | Ni | Si | Mn | P | S | Fe |
|-------|------|------|------|------|------|------|------|-------|------|------|-------|--------|------|
| | 0.05 | 18.5 | <0.1 | 2.95 | 5.11 | 0.97 | 0.51 | 52.45 | 0.07 | 0.06 | 0.004 | <0.001 | Bal. |

The Concept Laser M2 machine (GE Additive, Cincinnati, OH, USA), capable of utilizing dual laser beams, was employed for the L-PBF process to fabricate IN718 specimens. The detailed laser parameters, as shown in Table 2, involved varying the laser power between 370 W, 380 W, and 390 W, while keeping the laser scan speed, hatch distance, and layer thickness constant at 600 mm/s, 0.1 mm, and 25 µm, respectively. To minimize anisotropy as well as thermal stress of the specimen, the laser scan direction was rotated by 67 degrees for each layer. A support structure with a height of 5 mm was set up, and a cylindrical specimen with a diameter of 13 mm and a length of 80 mm was built on the support structure. As-built specimens were wire-cut from the base plate, each specimen was divided into eight equal parts with 10 mm intervals, as shown in Figure 1, denoted as bottom (No. 1,2), middle (No. 4,5), and top (No. 7,8), to observe the porosity fraction and initial microstructure according to the sample position. The porosity fraction was quantified using image analysis (Image-Pro Plus, Media Cybernetics, Rockville, MD, USA) after grinding with sandpaper, polishing with 1 µm diamond paste, and capturing optical microscope images at 10× magnification without etching. The amount of residual stress in the as-built specimens was

examined by the XRD $-\sin^2\psi$ method using XStress-3000 G3 [20,21]. This method could evaluate the residual stress from the change of lattice spacing with different tilting angle (ψ). The residual stress was calculated based on the following equation,

$$\frac{d_{\Phi\Psi} - d_0}{d_0} = \left(\frac{1 + \nu}{E}\right) \cdot \sigma_{\Phi} \cdot \sin^2(\Psi) - \frac{\nu}{E} \cdot (\sigma_1 + \sigma_2) \quad (1)$$

where $d_{\Phi\psi}$, d_0 , E , and ν stand for the lattice spacing of the (hkl) plane, lattice spacing of stress-free state, the Young's modulus, and Poisson's ratio, respectively. Equation (1) can be rewritten as follows by assuming that $\sigma_1 = \sigma_2$, and σ_{Φ} is independent of orientation.

$$d_{\Phi\Psi} = \left[\left(\frac{1 + \nu}{E}\right) \cdot \sin^2(\Psi) - \left(\frac{2\nu}{E}\right) \right] \cdot \sigma \cdot d_0 + d_0 \quad (2)$$

Therefore, it is possible to establish a linear explanation between $d_{\Phi\psi}$ ($= \lambda/2\sin\theta$) and $\left[\left(\frac{1+\nu}{E}\right) \cdot \sin^2(\Psi) - \left(\frac{2\nu}{E}\right) \right]$, which in turn allows us to obtain values of in-plane stress (σ) and d_0 . In this study, Cr-K α radiation was used, and eight different tilting angles ranging from -45 degrees to $+45$ degrees were employed around the $(220)_{\gamma}$ peak. The stress-relief heat treatment was conducted at 1065 °C, 1080 °C, and 1095 °C for 90 min to avoid precipitation of δ -phase (Ni_3Nb , D0_a), with a reference standard heat treatment following ASTM F3055 [22]. The aging heat treatment was performed according to AMS 5596, with a hold at 718 °C for 8 h [23]. It was then furnace-cooled down to 621 °C and held for an additional 8 h, followed by air cooling. The recrystallization after heat treatment was examined by performing electron backscatter diffraction (EBSD) (Oxford instruments, Abingdon, UK) with an acceleration voltage of 15 kV, and a step size of 4 μm . The observation was carried out on an area of 2560×1900 μm^2 of the plane normal to the building direction, as shown in Figure 1. The acquired data were post-processed using TSL-OIM software (version 7.3.1, EDAX, Mahwah, NJ, USA) with a filtering criterion applied to utilize only values with confidence index greater than 0.1 and grain size exceeding 3 μm .

Table 2. Laser powder bed fusion parameters for IN718 used in the present study.

| Laser Power | Spot Size | Scan Speed | Hatch Distance | Layer Thickness | Atmosphere |
|-------------|-------------------|------------|-------------------|------------------|------------|
| 370 W | 180 μm | 600 mm/s | 100 μm | 25 μm | Ar purging |
| 380 W | | | | | |
| 390 W | | | | | |

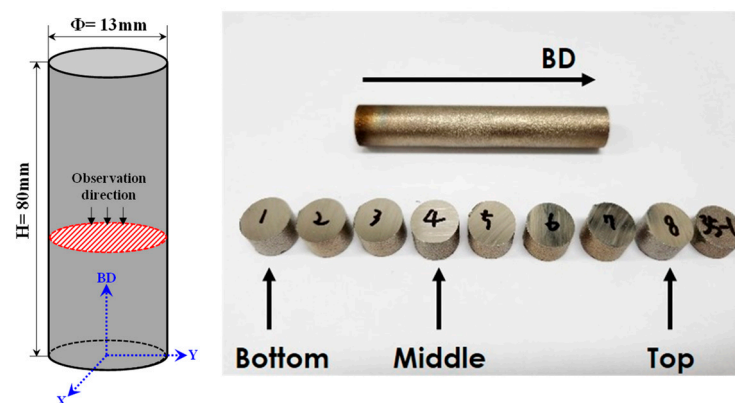


Figure 1. Sample location and observation direction for microstructure analysis.

Based on the grain orientation spread (GOS) value, grains with less than 1 degree deviation from the mean orientation were considered to be recrystallized grain. Finally, the fraction of the recrystallized grains was deduced by calculating the area fraction of grains

with the GOS value under 1 degree. The dislocation cell structure of the as-built specimen depending on laser power was observed using a transmission electron microscope (TEM, JEM-2100F, JEOL, Tokyo, Japan). The TEM sample was prepared with a 3 mm disc of 50 μm in thickness, followed by jet-polishing. The observation was performed after tilting the sample, aligning the incident beam parallel to the $\langle 001 \rangle_\gamma$ direction.

3. Results

3.1. Microstructure of As-Built Specimens

The porosity was measured on the plane perpendicular to the building direction (XY plane) of bottom, middle, and top region of each specimen. For the 370 W condition, the specimens were measured to have 0.621%, 0.787%, 1.263% of porosity at the bottom, middle, and top regions, respectively. Under the 380 W condition, the measurements were 2.457%, 3.597%, 4.955% at the bottom, middle, and top regions, respectively. Additionally, for the 390 W condition, the measurements were 3.201%, 2.581%, 2.914% at the bottom, middle, and top regions, respectively. The energy densities under these three conditions were higher than the optimal energy density provided by the powder supplier, indicating an increase in the key-hole fraction compared to defect fraction under the optimum laser parameter set [24]. Figure 2 presents the melt pool size and shape of the as-built specimens, observed at the plane perpendicular to laser scan direction. The average width and depth of the melt pool, measured at more than 10 different points, are denoted in the top-left corner of each optical micrograph. Generally, it is reported that the width and depth of the melt pool tend to increase simultaneously with increasing laser power, resulting in a larger volume. However, in this experiment, it was found that the width remained nearly constant or decreased slightly, whereas the depth of melt pool continuously increased as the laser power increased. As a result, the shape of melt pool changes from a shallow shape to a deep shape while maintaining the width.

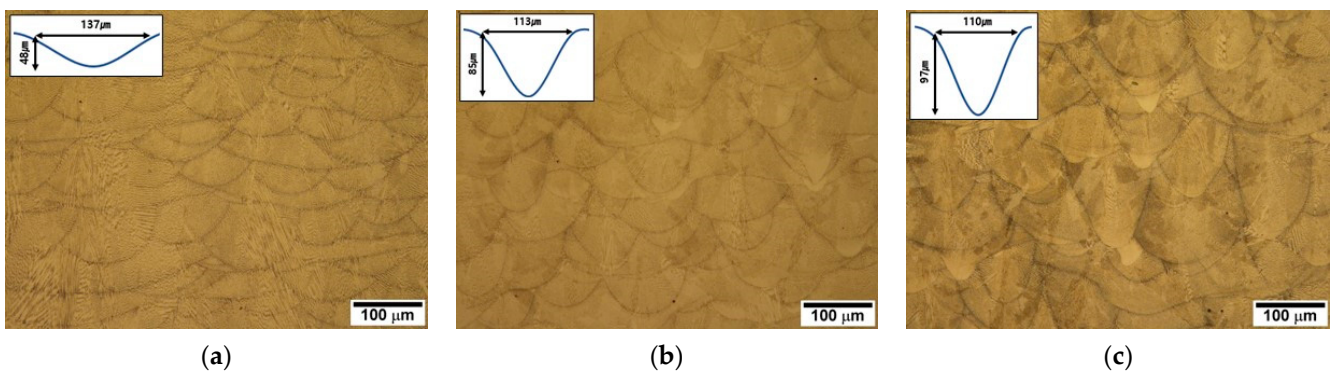


Figure 2. Melt pool size and shape observed at the plane normal to the scan direction: (a) 370 W; (b) 380 W; (c) 390 W.

Figure 3 illustrates the EBSD results obtained from the bottom region of the as-built specimens. One could notice from the inverse pole figure (IPF) map that multiple grains exhibit a regular alignment along the laser scan direction, which was rotated by 67 degrees every single layer. The positions of the observed (001) poles in the pole figure indicate that (001) poles are located either parallel or perpendicular to the laser scan direction. Moreover, a weak cube texture is discernible in the as-built specimens, and the maximum intensity of the poles diminishes as the laser power increases. However, this characteristic can vary depending on the surface location examined in EBSD imaging, whether it is at the intermediate depth of the layer or at the boundary between layers. Therefore, it is difficult to find the exact relationship between laser power and texture development in the present results. Nevertheless, considering the relationship between the laser scan direction and the position of the (001) poles, it is inferred that the overall as-built specimen exhibits a {001} fiber texture.

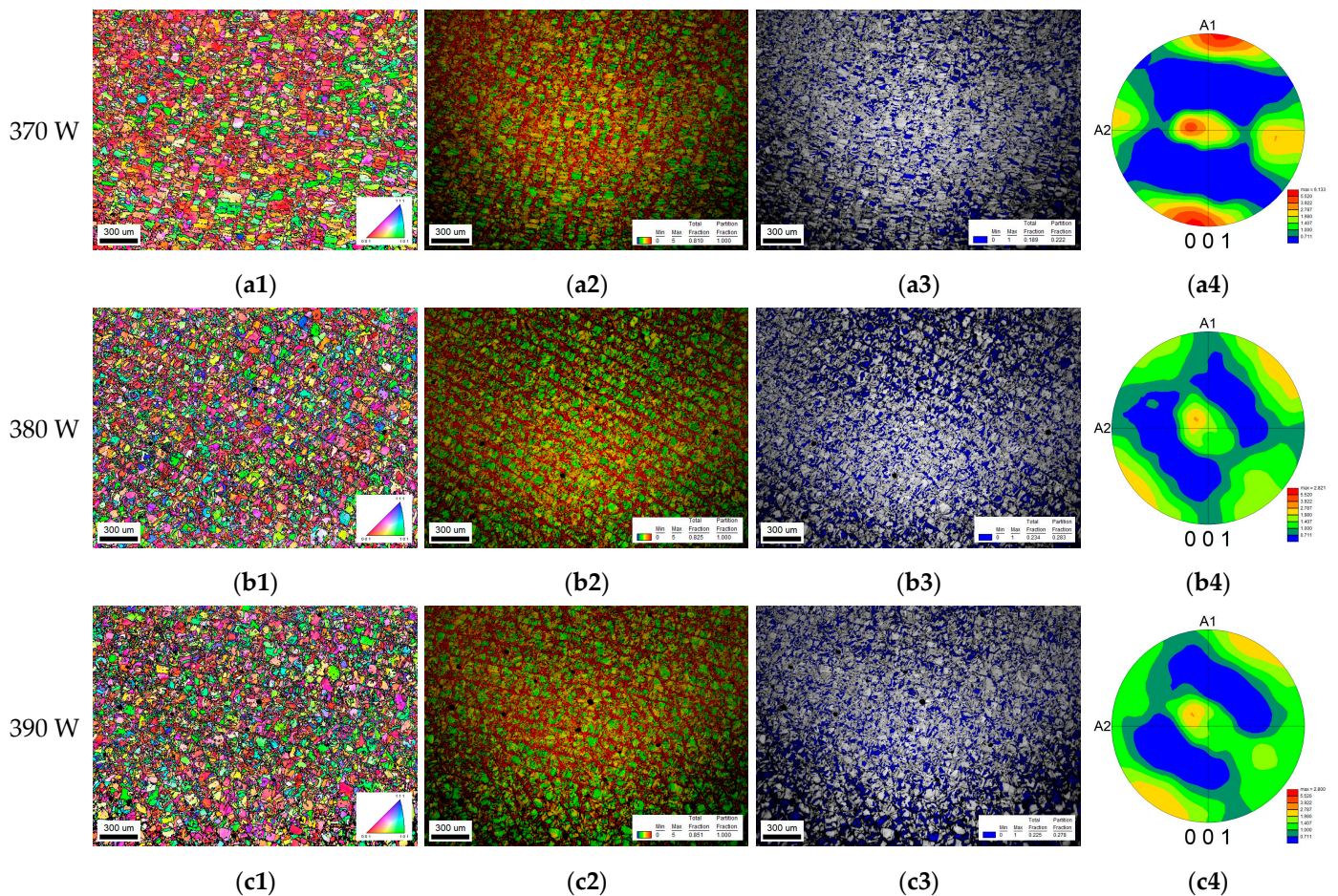


Figure 3. Electron backscattered diffraction images at the XY plane of as-built specimens: (a1,b1,c1) inverse pole figure map; (a2,b2,c2) kernel average misorientation map; (a3,b3,c3) image quality map with highlighting GOS under 1 degree; and (a4,b4,c4) pole figure map.

The KAM is a measure of the difference in orientation between a certain point and its surroundings. By maintaining a constant step size, KAM can be used as an indication of the relative deformation received during the additive manufacturing process. In the KAM map, alternating green and red bands represent low and high KAM values, respectively. This alternating pattern is also associated with the width of the melt pool and the hatch distance. Specifically, during the solidification of the melt pool, the surrounding region experiences tensile stresses due to solidification shrinkage of the melt pool. Consequently, higher deformation occurs in the boundary region of the melt pool compared to its central part, resulting in higher KAM values at the edges of the melt pool. However, the average KAM values measured in the observed area showed no significant trend with respect to laser power, with values of 3.248, 3.314, and 3.141 for 370, 380, and 390 W, respectively. Therefore, there are limitations in determining the driving force for recrystallization with increasing laser power based on the EBSD test condition performed in this study.

The thermal stresses generated during the L-PBF process can persist elastically even after plastic deformation occurred during rapid cooling [25–29]. This residual stress was measured in the bottom region of specimens fabricated under conditions of 370 W, 380 W, and 390 W, with the corresponding results depicted in Figure 4. It was observed that all measured specimens exhibited tensile residual stress, and as the laser power increased from 370 W to 390 W, with a 20 W increment, the residual stresses escalated from 195.6 MPa to 433.3 MPa. This result indicates the occurrence of higher thermal stresses with increasing laser power.

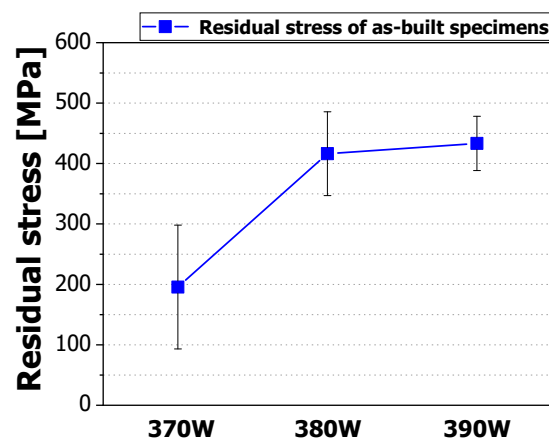


Figure 4. Residual stress of the as-built specimens measured from the bottom region.

3.2. Microstructure of Heat-Treated Specimens

The bottom region of the as-built specimens was subjected to stress-relief heat treatment in an argon atmosphere at temperatures of 1065 °C, 1080 °C, and 1095 °C, and the resulting microstructural changes were observed. Figure 5 presents the EBSD microstructure observations for a laser power of 370 W with increasing stress-relief heat treatment temperatures. Even after heat treatment, the laser scan path remains visible in both the IPF map and the KAM map. In addition, there was no significant change in the average KAM value within the measured area as the heat treatment temperature increased, with values of 2.887, 3.037, and 3.148. Furthermore, the recrystallized grain fraction based on the GOS value was 22.9%, 18.0%, and 16.9%, respectively. Assuming that the recrystallization temperature is where more than 50% of the total area undergoes recrystallization, the recrystallization temperature under the laser power condition of 370 W was found to be above 1095 °C.

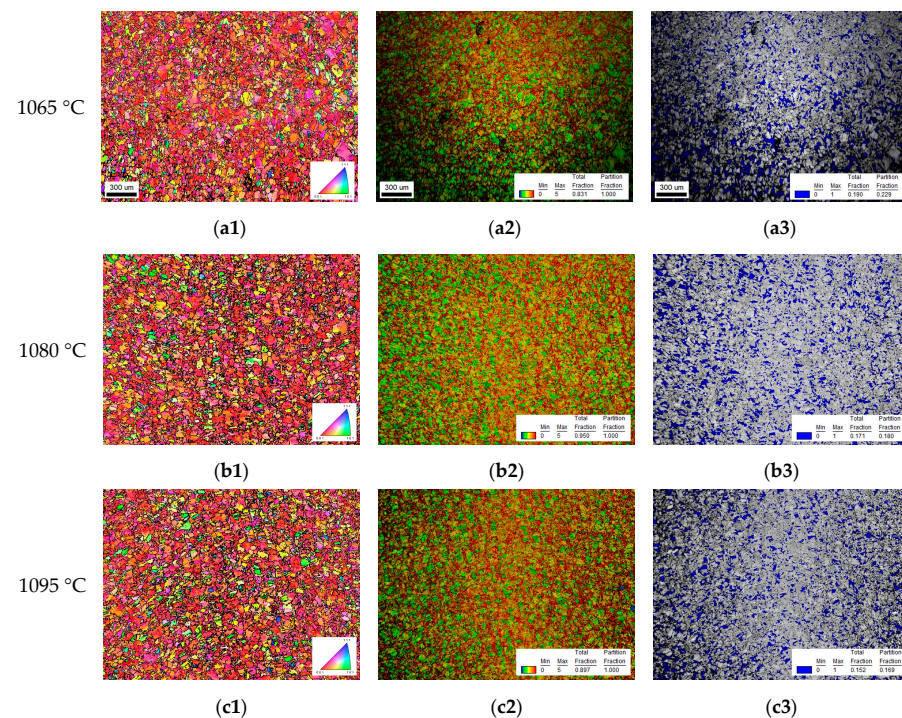


Figure 5. EBSD images for 370 W specimens with different stress-relief heat treatment temperatures: (a1,b1,c1) inverse pole figure map; (a2,b2,c2) kernel average misorientation map; (a3,b3,c3) image quality map highlighting GOS under 1 degree.

Similarly, specimens manufactured using a laser power of 380 W underwent heat treatment at the same three temperatures, and the resulting EBSD microstructure observations are displayed in Figure 6. Under the 380 W condition, the laser scan path remained clearly visible across all heat treatment conditions. The average KAM values for the entire map were found to be 3.103, 3.104, and 2.796, respectively, as the temperature increased. Notably, after heat treatment at 1080 °C and 1095 °C, the occurrence of local recrystallization became evident, as indicated by the yellow arrows in Figure 6a1–b3. Additionally, the recrystallized grain fractions based on the GOS values measured at 1065 °C, 1080 °C, and 1095 °C were 41.4%, 33.3%, and 47.1%, respectively. It is inferred that the recrystallization temperature for specimens under the laser power condition of 380 W approaches 1095 °C.

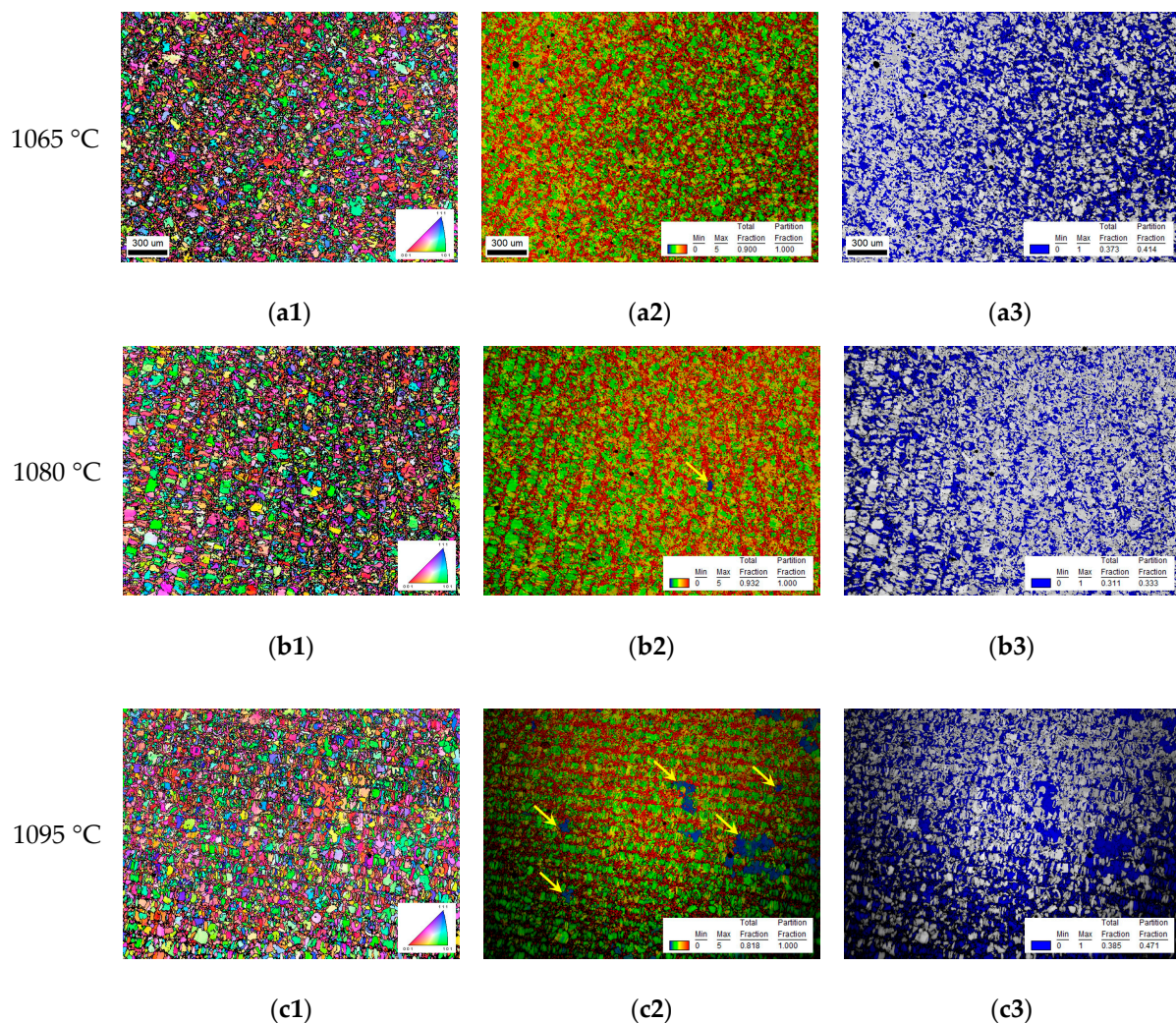


Figure 6. EBSD images for 380 W specimens with different stress-relief heat treatment temperatures: (a1,b1,c1) inverse pole figure map; (a2,b2,c2) kernel average misorientation map; (a3,b3,c3) image quality map with highlighting GOS under 1 degree.

On the other hand, the specimens produced with a laser power of 390 W maintained a lower recrystallized grain fraction of 10.3% after heat treatment at 1065 °C, as shown in Figure 7. In contrast, after heat treatment at 1080 °C and 1095 °C, a significant increase in the fraction of recrystallized grains can be found with values of 85.4% and 94.4%, respectively. As recrystallization progressed, the average KAM value within the measured area exhibited a significant decrease, reaching 3.332, 0.962, and 0.351 for 1065 °C, 1080 °C, and 1095 °C, respectively. Hence, it was confirmed that under the laser power condition of 390 W, the recrystallization temperature of the specimen exists between 1065 °C and 1080 °C.

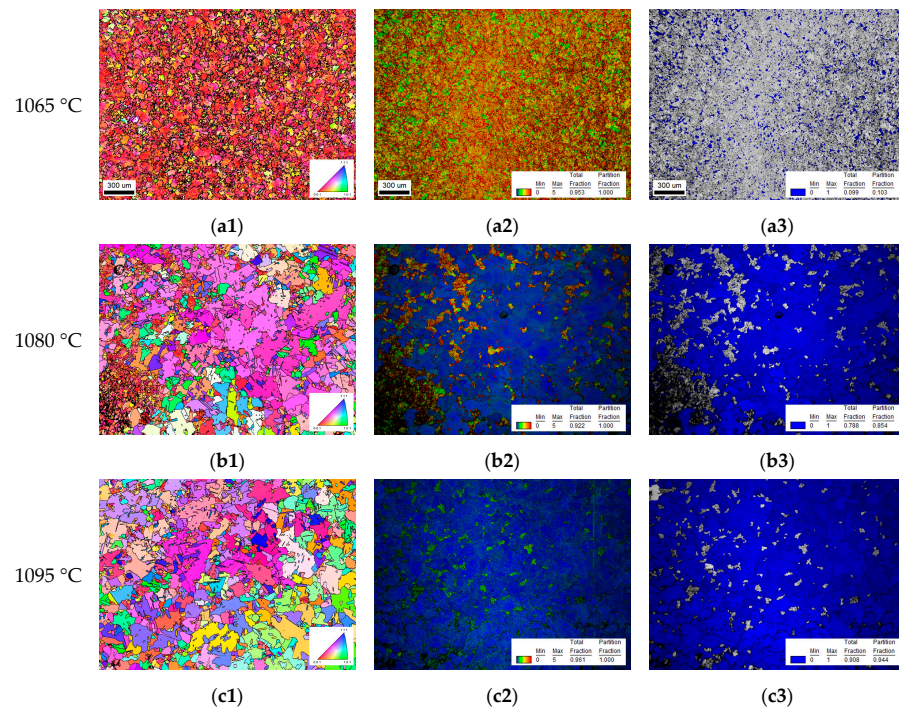


Figure 7. EBSD images for 390 W specimens with different stress-relief heat treatment temperatures: (a1,b1,c1) inverse pole figure map; (a2,b2,c2) kernel average misorientation map; (a3,b3,c3) image quality map with highlighting GOS under 1 degree.

Figure 8 demonstrates the fraction of recrystallized grain as a function of laser power and heat treatment temperature. By considering the recrystallization condition as when more than 50% of the measured area is converted to recrystallized grains, recrystallization occurred only at 1080 °C and 1095 °C after heat treatment under 390 W. Thus, it can be inferred that the recrystallization temperature is above 1095 °C for a laser power of 370 W, approximately 1095 °C for a laser power of 380 W, and between 1065 °C and 1080 °C for a laser power of 390 W.

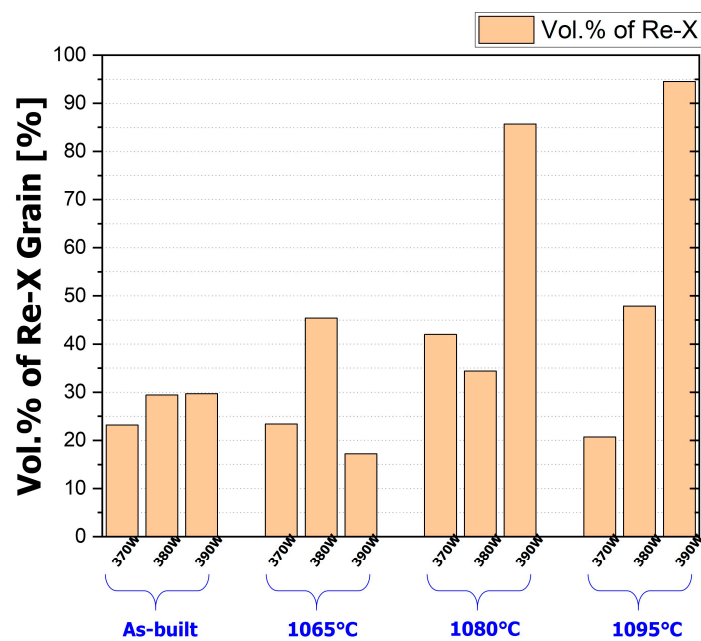


Figure 8. Volume fraction of recrystallized grain as a function of laser power and stress-relief heat treatment temperatures.

4. Discussion

4.1. Driving Force for Recrystallization Accumulated during Laser Powder Bed Fusion

The recrystallization observed in the additively manufactured materials can be attributed to various driving forces [28,30,31]. These forces encompass tensile deformation caused by solidification shrinkage around the melt pool, as well as accumulated tensile and compressive deformations arising from repetitive heating and cooling cycles. The resulting thermal stresses should be relaxed through various relaxation processes, including plastic deformation, solidification cracking, and liquation cracking. However, some stresses within the elastic limit at the particular temperature of a given material may persist as residual stress. Therefore, to comprehend the driving force for recrystallization in relation to the laser power, an evaluation of the factors influencing thermal stress is imperative.

It is widely recognized that the thermal stresses arising during the L-PBF process, under the identical material, equipment, and atmosphere conditions, are considerably influenced by the cooling rate of the melt pool. In essence, a higher cooling rate promotes thermal stress, whereas a relatively lower cooling rate results in reduced thermal stress.

The cooling rate of the melt pool is dependent on the volume of the melt pool [32,33]. Under a constant temperature gradient, an increase in the melt pool's volume prolongs the required solidification time, consequently reducing the cooling rate. Previous studies have indicated that with increasing laser power, both the width and depth of the melt pool tend to increase, leading to a larger volume of the melt pool and, subsequently, a diminished cooling rate. The cooling rate is also influenced by the heat transfer from the melt pool to its surroundings [34,35]. A more pronounced heat transfer from the melt pool can provide a higher cooling rate and rapid solidification. This factor is contingent upon various factors, including the heat capacity of the melt pool, heat transfer mechanisms, heat transfer coefficients, and the surface area per unit volume of the melt pool. Furthermore, the cooling rate is affected by additional factors such as the geometry of the build, support structure, the scan strategy, and the characteristics of the chamber [36–39].

4.2. Driving Force for Recrystallization with Increasing Laser Power

The experimental results confirm that the recrystallization temperature exhibits a downward trend as the laser power increases, indicating an increase in the driving force for recrystallization. It can be expected that the cooling rate of the melt pool increases with increasing laser power. The changes in the dimensions of the melt pool with respect to laser power, as shown in Figure 2, clearly demonstrate that the volume of the melt pool expands with higher laser power, while the width remains constant or slightly decreases, and only the depth experiences an increase. The amount of heat transfer, therefore, tends to increase with a deeper melt pool shape compared to a shallower one. Consequently, it can be deduced that a larger amount of heat dissipation occurs due to the higher surface area per unit volume of the melt pool, resulting in a faster cooling rate with increasing laser power.

To verify this, TEM observation of the as-built specimens at different laser powers were carried out and are presented in Figure 9. By setting the zone axis to $\langle 001 \rangle_{\gamma}$, the average cell size was measured, resulting in 707 nm for 370 W, 648 nm for 380 W, and 518 nm for 390 W. These measurement correspond to the increasing trend in heat dissipation of the melt pool with higher laser power, suggesting a faster cooling rate. Additionally, the presence of the dislocation cell structure formed at the cell boundaries was observed. This dislocation cell structure is known to form as a result of repetitive heating and cooling, which leads to tensile and compressive deformation even after solidification. Notably, it can be clearly observed that the dislocation density formed at the cell boundaries increases with increasing laser power.

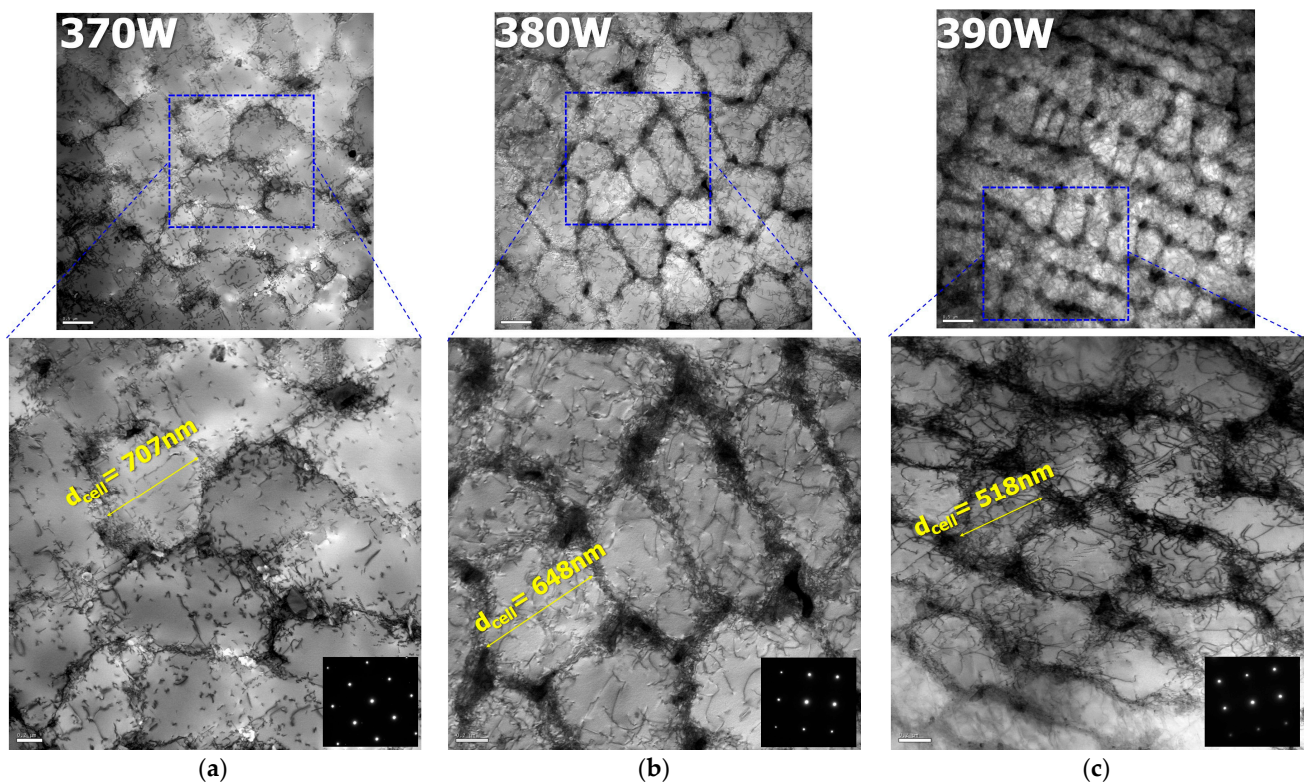


Figure 9. Dislocation cell structure of the as-built specimens with the zone axis of $\langle 001 \rangle_{\gamma}$: (a) 370 W; (b) 380 W; (c) 390 W.

5. Conclusions

In this study, we investigated the variation in the recrystallization temperature of L-PBF IN718 specimens as a function of laser power. By applying three stress-relief heat treatment temperatures, we were able to clearly distinguish the temperature ranges in which recrystallization occurred under different laser powers. Through various microstructure analyses, we discovered evidence that the reason for the increasing driving force of recrystallization with increased laser power.

1. The observation plane of the as-built specimens exhibited a weak cube texture, with (001) planes aligned perpendicular or parallel to the laser scan path. The average KAM values, under the EBSD conditions used in this study, showed minimal differences based on laser power. However, the residual stresses increased by more than two times as the laser power increased from 370 W to 390 W.
2. By defining the recrystallization temperature based on the area of the recrystallized region after stress-relief heat treatment, we found that the recrystallization temperature was above 1095 °C for 370 W, approximately 1095 °C for 380 W, and within the range of 1065–1080 °C for 390 W. This confirmed that the recrystallization temperature decreased with increasing laser power.
3. Thermal stress resulting from rapid cooling during the L-PBF process is one of the major driving forces for recrystallization. On the basis of the recrystallization temperature, it can be inferred through microstructure analysis that the 390 W condition experienced the fastest cooling rate due to pronounced heat dissipation from the melt pool. TEM observations indeed revealed the smallest cell size under the 390 W condition, indicating a faster cooling rate. Additionally, the highest dislocation density, resulting from repetitive heating and cooling even after solidification, was observed at 390 W, suggesting the highest driving force for recrystallization.

Author Contributions: Conceptualization, J.E.J. and Y.S.C.; methodology, D.H.S., J.E.J. and Y.S.C.; software, B.-G.C. and J.D.; validation, D.H.S., I.S.K., B.-G.C., J.D., Y.S.C. and J.E.J.; formal analysis, I.S.K. and J.D.; investigation, D.H.S. and J.E.J.; resources, D.H.S., J.D. and B.-G.C.; data curation, D.H.S., Y.S.C. and J.E.J.; writing—original draft preparation, D.H.S.; writing—review and editing, J.E.J. and Y.S.C.; visualization, D.H.S. and J.E.J.; supervision, Y.S.C. and J.E.J.; project administration, B.-G.C. and J.E.J.; funding acquisition, B.-G.C. and J.E.J. All authors have read and agreed to the published version of the manuscript.

Funding: This research was funded by Fundamental Research Program (PNK8890) of the Korea Institute of Materials Science (KIMS).

Data Availability Statement: No new data were created or analyzed in this study. Data sharing is not applicable to this article.

Conflicts of Interest: The authors declare no conflict of interest.

References

1. DebRoy, T.; Wei, H.L.; Zuback, J.S.; Mukherjee, T.; Elmer, J.W.; Milewski, J.O.; Beese, A.M.; Wilson-Heid, A.D.; De, A.; Zhang, W. Additive manufacturing of metallic components—Process, structure and properties. *Prog. Mater. Sci.* **2018**, *92*, 112–224. [[CrossRef](#)]
2. Blakey-Milner, B.; Gradl, P.; Snedden, G.; Brooks, M.; Pitot, J.; Lopez, E.; Leary, M.; Berto, F.; Du Plessis, A. Metal additive manufacturing in aerospace: A review. *Mater. Des.* **2021**, *209*, 110008. [[CrossRef](#)]
3. Dai, K.; Shaw, L. Thermal and stress modeling of multi-material laser processing. *Acta Mater.* **2001**, *499*, 4171. [[CrossRef](#)]
4. Giuliani, F.; Paulitsch, N.; Cozzi, D.; Görtler, M.; Andracher, L. An assessment on the benefits of additive manufacturing regarding new swirler geometries for gas turbine burners. In Proceedings of the ASME Turbo Expo 2018, Oslo, Norway, 11–15 June 2018.
5. Prabhakar, P.; Sames, W.J.; Dehoff, R.; Babu, S.S. Computational modeling of residual stress formation during the electron beam melting process for Inconel 718. *Addit. Manuf.* **2015**, *7*, 83–91. [[CrossRef](#)]
6. Kok, Y.; Tan, X.P.; Wang, P.; Nai, M.L.S.; Loh, N.H.; Liu, E.; Tor, S.B. Anisotropy and heterogeneity of microstructure and mechanical properties in metal additive manufacturing: A critical review. *Mater. Des.* **2018**, *139*, 565–586. [[CrossRef](#)]
7. Park, J.M.; Asghari-Rad, P.; Zargaran, A.; Bae, J.W.; Moon, J.; Kwon, H.; Choe, J.; Yang, S.; Yu, J.H.; Kim, H.S. Nano-scale heterogeneity-driven metastability engineering in ferrous medium-entropy alloy induced by additive manufacturing. *Acta Mater.* **2021**, *221*, 117426. [[CrossRef](#)]
8. Han, J.; Yang, J.; Yu, H.; Yin, J.; Gao, M.; Wang, Z.; Zeng, X. Microstructure and mechanical property of selective laser melted Ti6Al4V dependence on laser energy density. *Rapid Prototyp. J.* **2017**, *23*, 217–226. [[CrossRef](#)]
9. Li, J.; Wei, Z. Process optimization and microstructure characterization of Ti6Al4V manufactured by selective laser melting. *IOP Conf. Ser. Mater. Sci. Eng.* **2017**, *269*, 012026.
10. Pal, S.; Gubeljak, N.; Hudák, R.; Lojen, G.; Rajčúková, V.; Brajljeh, T.; Drstvenšek, I. Evolution of the metallurgical properties of Ti-6Al-4V, produced with different laser processing parameters, at constant energy density in selective laser melting. *Results Phys.* **2020**, *17*, 103186. [[CrossRef](#)]
11. Sonis, E.; Dépinoy, S.; Giroux, P.; Maskrot, H.; Lemarquis, L.; Hercher, O.; Villaret, F.; Gourgues-Lorenzon, A. Dependency of recrystallization kinetics of the solidification microstructure of 316L stainless steel processed by laser powder bed fusion (LPBF). *Mater. Char.* **2022**, *194*, 112370. [[CrossRef](#)]
12. De Terris, T.; Castelnau, O.; Hadjem-Hamouche, Z.; Haddadi, H.; Michel, V.; Peyre, P. Analysis of As-built microstructures and recrystallization phenomena on Inconel 625 alloy obtained via laser powder bed fusion (L-PBF). *Metals* **2021**, *11*, 619. [[CrossRef](#)]
13. Pinto, F.C.; Aota, L.S.; Souza Filho, I.R.; Raabe, D.; Sandim, H.R.Z. Recrystallization in non-conventional microstructures of 316L stainless steel produced via laser powder-bed fusion: Effect of particle coarsening kinetics. *J. Mater. Sci.* **2022**, *57*, 9576–9598. [[CrossRef](#)]
14. Jiang, R.; Mostafaei, A.; Wu, Z.; Choi, A.; Guan, P.W.; Chmielus, M.; Rollett, A.D. Effect of heat treatment on microstructural evolution and hardness homogeneity in laser powder bed fusion of alloy 718. *Addit. Manuf.* **2020**, *35*, 101282. [[CrossRef](#)]
15. Pröbstle, M.; Neumeier, S.; Hopfenmüller, J.; Freund, L.P.; Niendorf, T.; Schwarze, D.; Göken, M. Superior creep strength of a nickel-based superalloy produced by selective laser melting. *Mater. Sci. Eng. A* **2016**, *674*, 299–307. [[CrossRef](#)]
16. Gallmeyer, T.G.; Moorthy, S.; Kappes, B.B.; Mills, M.J.; Amin-Ahmadi, B.; Stebner, A.P. Knowledge of process-structure-property relationships to engineer better heat treatments for laser powder bed fusion additive manufactured Inconel 718. *Addit. Manuf.* **2020**, *31*, 100977. [[CrossRef](#)]
17. Zhao, Y.; Meng, F.; Liu, C.; Tan, S.; Xiong, W. Impact of homogenization on microstructure-property relationships of Inconel 718 alloy prepared by laser powder bed fusion. *Mater. Sci. Eng. A* **2021**, *826*, 141973. [[CrossRef](#)]
18. Doğu, M.N.; Davut, K.; Obeidi, M.A.; Yalçın, M.A.; Gu, H.; Low, T.S.E.; Ginn, J.; Brabazon, D. Recrystallization and grain growth kinetics of IN718 manufactured by laser powder bed fusion. *J. Mater. Res. Technol.* **2022**, *19*, 4242–4257. [[CrossRef](#)]
19. Praveen Kumar, V.; Vinoth Jebaraj, A. Microscale investigations on additively manufactured Inconel 718: Influence of volumetric energy density on microstructure, texture evolution, defects control and residual stress. *App. Phys. A* **2023**, *129*, 370. [[CrossRef](#)]

20. Macherauch, E. X-ray stress analysis. *Exptl. Mech.* **1966**, *6*, 140–153. [[CrossRef](#)]
21. Mirkoohi, E.; Tran, H.C.; Lo, Y.L.; Chang, Y.C.; Lin, H.Y.; Liang, S.Y. Mechanics modeling of residual stress considering effect of preheating in laser powder bed fusion. *J. Manuf. Mater. Process.* **2021**, *5*, 46. [[CrossRef](#)]
22. *ASTM F3055-14a*; Standard Specification for Additive Manufacturing Nickel Alloy (UNS NO7718) with Powder Bed Fusion. ASTM International: West Conshohocken, PA, USA, 2014.
23. *AMS 5596E*; Aerospace Material Specification for Inconel 718 (UNS NO7718) Sheets, Strips and Plates. Society for Automotive Engineers: Warrendale, PA, USA, 1984.
24. Giorgetti, A.; Baldi, N.; Palladino, M.; Ceccanti, F.; Arcidiacono, G.; Citti, P. A method to optimize parameters development in L-PBF based on single and multitracks analysis: A case study on Inconel 718 alloy. *Metals* **2023**, *13*, 306. [[CrossRef](#)]
25. Bartlett, J.L.; Li, X. An overview of residual stresses in metal powder bed fusion. *Addit. Manuf.* **2019**, *27*, 131–149. [[CrossRef](#)]
26. Levkulich, N.C.; Semiatin, S.L.; Gockel, J.E.; Middendorf, J.R.; DeWald, A.T.; Klingbeil, N.W. The effect of process parameters on residual stress evolution and distortion in the laser powder bed fusion of Ti-6Al-4V. *Addit. Manuf.* **2019**, *28*, 475–484. [[CrossRef](#)]
27. Chen, C.; Xiao, Z.; Zhang, W.; Wang, Y.; Zhu, H. Effect of laser jump speed on temperature distribution and thermal stress in laser powder bed fusion. *Opt. Laser Technol.* **2021**, *142*, 107275. [[CrossRef](#)]
28. Mirkoohi, E.; Tran, H.C.; Lo, Y.L.; Chang, Y.C.; Lin, H.Y.; Liang, S.Y. Analytical modeling of residual stress in laser powder bed fusion considering part's boundary condition. *Crystals* **2020**, *10*, 337. [[CrossRef](#)]
29. Gan, M.; Wu, Q.; Long, L. Prediction of residual deformation and stress of laser powder bed fusion manufactured Ti-6Al-4V lattice structures based on inherent strain method. *Mater. Res.* **2023**, *26*, e20220516. [[CrossRef](#)]
30. Ulbricht, A.; Altenburg, S.J.; Sprengel, M.; Sommer, K.; Mohr, G.; Fritsch, T.; Mishurova, T.; Serrano-Munoz, I.; Evans, A.; Hofmann, M.; et al. Separation of the formation mechanisms of residual stresses in LPBF 316L. *Metals* **2020**, *10*, 1234. [[CrossRef](#)]
31. Antikainen, A.; Reijonen, J.; Lagerbom, J.; Lindroos, M.; Pinomaa, T.; Lindroos, T. Experimental and Calphad methods for evaluating residual stresses and solid-state shrinkage after solidification. *Metals* **2022**, *12*, 1894. [[CrossRef](#)]
32. Zhang, Z.; Ali, U.; Mahmoodkhani, Y.; Huang, Y.; Shahabad, S.I.; Kasinathan, A.R.; Toyserkani, E. Experimental and numerical investigation on the effect of layer thickness during laser powder-bed fusion of stainless steel 17-4 PH. *Int. J. Rapid Manuf.* **2020**, *9*, 212–230. [[CrossRef](#)]
33. Farshidianfar, M.H.; Khajepour, A.; Gerlich, A.P. Effect of real-time cooling rate on microstructure in laser additive manufacturing. *J. Mater. Proc. Technol.* **2016**, *231*, 468–478. [[CrossRef](#)]
34. Chai, R.; Zhang, Y.; Zhong, B.; Zhang, C. Effect of scan speed on grain and microstructural morphology for laser additive manufacturing of 304 stainless steel. *Rev. Adv. Mater. Sci.* **2021**, *60*, 744–760. [[CrossRef](#)]
35. Hyer, H.C.; Petrie, C.M. Effect of powder layer thickness on the microstructural development of additively manufactured SS316. *J. Manuf. Proc.* **2022**, *76*, 666–674. [[CrossRef](#)]
36. Chua, Z.Y.; Moon, S.K.; Jiao, L.; Ahn, I.H. Geometric influence of the laser-based powder bed fusion process in Ti6Al4V and AlSi10Mg. *Int. Adv. Manuf. Technol.* **2021**, *114*, 3165–3176. [[CrossRef](#)]
37. Song, H.; McGaughy, T.; Sadek, A.; Zhang, W. Effect of structural support on microstructure of nickel base superalloy fabricated by laser powder bed fusion additive manufacturing. *Addit. Manuf.* **2019**, *26*, 30–40. [[CrossRef](#)]
38. Ekubaru, Y.; Gokcekaya, O.; Nakano, T. Effects of scanning strategy on the microstructure and mechanical properties of Sc-Zr-modified Al-Mg alloy manufactured by laser powder bed fusion. *Crystals* **2022**, *12*, 1348. [[CrossRef](#)]
39. Sun, Q.; Guo, K.; Wang, X.; Liu, J.; Sun, J. Effect of scanning strategies on the microstructure and mechanical behavior of 316L stainless steel fabricated by selective laser melting. *Mater. Sci. Eng. A* **2020**, *793*, 139879.

Disclaimer/Publisher's Note: The statements, opinions and data contained in all publications are solely those of the individual author(s) and contributor(s) and not of MDPI and/or the editor(s). MDPI and/or the editor(s) disclaim responsibility for any injury to people or property resulting from any ideas, methods, instructions or products referred to in the content.